





Denoising of imaginary time response functions with Hankel projections

Yang Yu ^{1,*}, Alexander F. Kemper ^{2,†}, Chao Yang ^{3,‡} and Emanuel Gull ^{1,§}

¹Department of Physics, University of Michigan, Ann Arbor, Michigan 48109, USA

²Department of Physics, North Carolina State University, Raleigh, North Carolina 27695, USA

³Computational Research Division, Lawrence Berkeley National Laboratory, Berkeley, California 94720, USA



(Received 19 March 2024; accepted 30 July 2024; published 23 August 2024)

Imaginary-time response functions of finite-temperature quantum systems are often obtained with methods that exhibit stochastic or systematic errors. Reducing these errors comes at a large computational cost—in quantum Monte Carlo simulations, the reduction of noise by a factor of two incurs a simulation cost of a factor of four. In this paper, we relate certain imaginary-time response functions to an inner product on the space of linear operators on Fock space. We then show that data with noise typically does not respect the positive definiteness of its associated Gramian. The Gramian has the structure of a Hankel matrix. As a method for denoising noisy data, we introduce an alternating projection algorithm that finds the closest positive definite Hankel matrix consistent with noisy data. We test our methodology at the example of fermion Green's functions for continuous-time quantum Monte Carlo data and show remarkable improvements of the error, reducing noise by a factor of up to 20 in practical examples. We argue that Hankel projections should be used whenever finite-temperature imaginary-time data of response functions with errors is analyzed, be it in the context of quantum Monte Carlo, quantum computing, or in approximate semianalytic methodologies.

DOI: [10.1103/PhysRevResearch.6.L032042](https://doi.org/10.1103/PhysRevResearch.6.L032042)

Introduction. A fundamental task in the study of quantum field theories is the evaluation of the expectation value of dynamical correlation functions in a statistical ensemble [1]. For most nontrivial models, these correlation functions cannot be evaluated analytically, and one has to resort to numerical methods of some form. Chief among these are quantum Monte Carlo (QMC) methods, which simulate field theories by stochastic sampling [2–13]. These methods form the backbone of correlated lattice model [14] and materials simulations [15] and are also used to study systems in high energy physics, such as quantum chromodynamics [8,16]. Many-body simulations of correlation functions on quantum computers are similarly of a statistical nature.

The predictive power of stochastic simulations of quantum field theories is often limited only by the precision to which correlation functions, such as Green's functions and susceptibilities, can be obtained. This precision is characterized by the size of the statistical error, which decreases only as the square root of the computational effort. Thus, decreasing the uncertainty comes at a high computational cost once some threshold in effort (and thus precision) has been reached.

The majority of statistical simulations of quantum field theories are performed in so-called imaginary time or Matsubara frequencies [17], though alternative numerically exact formulations based on Keldysh diagrammatics [10,18–20] are possible on small systems. In the absence of a sign problem, this Wick-rotated formalism results in positive real simulation weights with a straightforward probabilistic interpretation. However, the interpretation of response functions requires an analytic continuation [21–23] that exponentially amplifies statistical and systematic uncertainties.

Given the high computational cost, it is of great benefit to identify components of the error that violate fundamental physical laws or mathematical constraints. For example, if a quantum computing simulation is known to have a fixed particle number, a sample that violates this constraint can be removed from consideration [24]. Causality, or the positivity of the spectral function, is another such physical criterion. Noisy real-time simulations can make use of a causal projection based on an inner product structure and a projection to an associated positive semidefinite (PSD) Toeplitz matrix, leading to vastly improved spectra of time-evolved systems [25].

This paper introduces a criterion based on an inner product structure for equilibrium imaginary-time correlation functions. We define an inner product of imaginary time (τ) operators on the Fock space and show its positivity. When discretized on a uniform grid, its Gramian matrix is a positive semidefinite Hankel matrix whose positivity may be violated in noisy simulations. We then devise an alternating projection algorithm to find the positive-semidefinite Hankel matrix closest to given noisy data and thereby denoise imaginary time data. In an application to numerical results from typical QMC

*Contact author: umyangyu@umich.edu

†Contact author: akemper@ncsu.edu

‡Contact author: cyang@lbl.gov

§Contact author: egull@umich.edu

problems, we find that this projection substantially reduces the statistical error at negligible computational cost.

Method. For a system described with a Hamiltonian H at inverse temperature β and with density matrix $\rho = e^{-\beta H}/\mathcal{Z}$ and partition function $\mathcal{Z} = \text{Tr}(e^{-\beta H})$, the real-time correlation function $G(t, t')$ of an operator $A^\dagger(t)$ with another operator $B(t')$,

$$G_{AB}(t, t') = \text{Tr}[\rho(e^{iHt} A^\dagger e^{-iHt})(e^{iHt'} B e^{-iHt'})], \quad (1)$$

induces an inner product $\langle A(t), B(t') \rangle$ on the vector space of linear operators $A(t), B(t')$ from the Fock space to itself, since it satisfies linearity, conjugate symmetry, and positivity when the operators are identical: $G_{AA}(t, t) = \langle A(t), A(t) \rangle \geq 0$ [25,26]. The operators A and B may be either fermionic or bosonic. As a consequence, for any sequence (t_1, t_2, \dots, t_N) , and for any operator A , the Gramian $\underline{G}_{ij} = G_{AA}(t_i, t_j)$, $1 \leq i, j \leq N$ is a positive semidefinite $N \times N$ matrix that can be used as a starting point for denoising real-time simulations [25]. Moreover, if the correlation function is time-translation invariant, i.e., $\underline{G}(t_i, t_j) = \underline{G}(t_i - t_j)$, the Gramian matrix is a Toeplitz matrix.

Consider, in analogy, the imaginary time function:

$$G_{AB}(\tau, \tau') = \text{Tr}[\rho(e^{\tau H} A^\dagger e^{-\tau H})(e^{-\tau' H} B e^{\tau' H})]. \quad (2)$$

This expression similarly satisfies linearity, conjugate symmetry, and for $0 \leq \tau + \tau' \leq \beta$, $G_{AB}(\tau, \tau')$ coincides with the definition of an imaginary time correlation function of $\tau + \tau'$:

$$G_{AB}(\tau, \tau') = G_{AB}(\tau + \tau') = G_{AB}(\tau', \tau). \quad (3)$$

Due to the time-ordering in the definition of the imaginary-time correlation function, this coincidence is only true inside the interval $0 \leq \tau + \tau' \leq \beta$.

The remaining requirement for $G_{AB}(\tau, \tau')$ to be an inner product, positivity, is straightforward. We define $A(\tau) = e^{-\tau H} A e^{\tau H}$ with $A^\dagger(\tau) = e^{\tau H} A^\dagger e^{-\tau H}$, such that $G_{AA}(\tau, \tau') = \text{Tr}[\rho A^\dagger(\tau) A(\tau')]$. We note that $B(\tau) = A^\dagger(\tau) A(\tau)$ is positive semidefinite since it is a product of a matrix and its adjoint. Thus, $G_{AA}(\tau, \tau) = \text{Tr}[\rho B(\tau)] \geq 0$ for any τ , since ρ is also PSD, and $\text{Tr}[PQ] \geq 0$ for any two PSD matrices P and Q . $G_{AB}(\tau, \tau')$ therefore forms an inner product $\langle A(\tau), B(\tau') \rangle$ on the space of linear operators from the Fock space to itself. Moving forward, we will focus on $G_{AA}(\tau, \tau')$, drop the subscript, and simply refer to $G(\tau, \tau')$.

As a consequence, for time points $(\tau_1, \tau_2, \dots, \tau_N)$ the Gramian matrix $\underline{H}_{ij} = G(\tau_i, \tau_j)$ is positive semidefinite. Moreover, if the time points are uniformly spaced at distance $\Delta\tau$, all antidiagonal entries of \underline{H} are identical and \underline{H} has the structure of a Hankel matrix. In that case, the Gramian matrix has entries $H_{ij} = G_{i+j} = G(\tau_i + \tau_j)$ with $\tau_i = i\Delta\tau$, $i = 0, \dots, N/2 = \beta/(2\Delta\tau)$ (N even). This matrix is illustrated in Fig. 1, and by the argument above it must be PSD. In addition, its submatrix with the first column and last row dropped (depicted with dashed lines in Fig. 1), which corresponds to time points $(\frac{\Delta\tau}{2}, \frac{3\Delta\tau}{2}, \dots, \frac{(N-1)\Delta\tau}{2})$, is also PSD.

Algorithm. A Hankel matrix \underline{H}_{ij} obtained from approximate or statistical simulations of a correlation function \tilde{G} is typically not PSD due to approximation errors or noise. It is therefore natural to construct the PSD Hankel matrix \underline{H}_{ij}

$$\underline{H} = \begin{pmatrix} G_0 & G_1 & G_2 & G_3 & \dots & G_{\frac{N}{2}-1} & G_{\frac{N}{2}} \\ G_1 & G_2 & G_3 & G_4 & \dots & & G_{\frac{N}{2}+1} \\ G_2 & G_3 & G_4 & G_5 & \dots & & \\ \vdots & \vdots & \vdots & \vdots & \ddots & \vdots & \vdots \\ G_{\frac{N}{2}-1} & & & & & G_{N-2} & G_{N-1} \\ G_{\frac{N}{2}} & G_{\frac{N}{2}+1} & & & & G_{N-1} & G_N \end{pmatrix}$$

FIG. 1. Hankel matrix $\underline{H}_{ij} = G_{i+j} = G(\tau_i + \tau_j)$ for $i, j = (0, 1, \dots, \frac{N}{2})$ used in the projection. Also shown (dashed line) is the Hankel matrix corresponding to $i, j = (\frac{1}{2}, \frac{3}{2}, \dots, \frac{N-1}{2})$.

that is closest to \tilde{H}_{ij} within an appropriately chosen norm, from which we can extract a denoised G . Here, we choose the Frobenius norm. Additionally, G should satisfy physical constraints, such as fermion or boson (anti)commutation relations or predetermined values at 0 and β .

Projection algorithm. Before outlining the procedure for finding G , we make the following observations regarding PSD and Hankel matrices.

(i) In the Frobenius norm, the closest PSD matrix to a given Hankel matrix is obtained by diagonalizing the matrix and setting all negative eigenvalues to zero [28]. The resulting matrix is in general not a Hankel matrix. PSD matrices form a convex set, since for any two PSD matrices P, Q and any $0 \leq \alpha \leq 1$ the matrix $A = \alpha P + (1 - \alpha)Q$ is also PSD; this follows straightforwardly from the observation that $x^T A x = \alpha x^T P x + (1 - \alpha)x^T Q x \geq 0$ for any vector x .

(ii) The closest Hankel matrix (in the Frobenius norm) to any positive matrix is obtained by averaging the antidiagonals [29]. The resulting matrix is in general not PSD. Hankel matrices also form a convex set since, for two Hankel matrices H_1 and H_2 , $H_3 = \alpha H_1 + (1 - \alpha)H_2$ is also a Hankel matrix.

(iii) Values of correlation functions at $\tau = 0$ or $\tau = \beta$ are often known to much higher precision than values at arbitrary times since they correspond to static expectation values. The $M \times M$ matrix \underline{B} ($M = \frac{N}{2} + 1$) with fixed values at the $(0,0)$ and/or (M, M) position closest to a given matrix \underline{A} is obtained simply by replacing the values of \underline{A} at $(0,0)$ and (M, M) by the desired values. If \underline{A} is a PSD Hankel matrix, \underline{B} retains the Hankel structure but is in general not PSD. The set of matrices with fixed values at $(0,0)$ and (M, M) is convex.

At least one positive definite Hankel matrix with a given value at $\tau = 0$ and β exists, since the exact solution to the problem satisfies these properties. Since the intersection of these convex sets is not empty, it is possible to use Dykstra's algorithm [30] (see also Appendix A) to find the intersection point of these convex sets closest to any given set of noisy data. Dykstra's algorithm repeatedly performs projections onto PSD matrices, onto the two Hankel matrices of Fig. 1, and onto matrices with fixed values at $(0,0)$ and (M, M) until convergence is achieved within a predefined tolerance. The PSD projections may enforce both the PSD structure of \underline{H} and the PSD structure of the submatrix illustrated in Fig. 1. While the convergence of the algorithm may be slow, for typical numbers of time slices (50–5000)

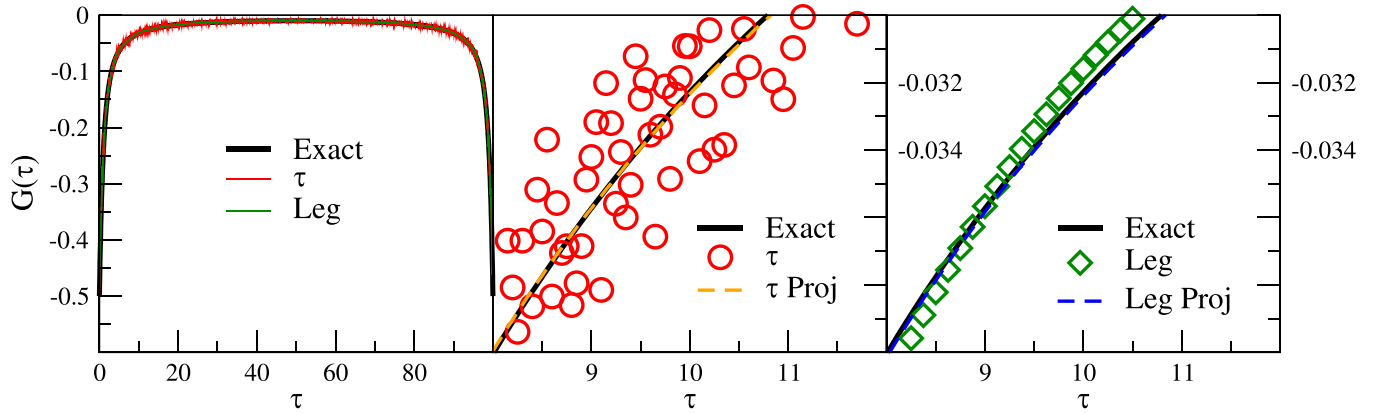


FIG. 2. Left panel: Imaginary time Green’s function corresponding to a semicircular density of states at $U = 0$ and $\beta = 100$ showing the exact data, data obtained with hybridization expansion continuous-time quantum Monte Carlo (CT-HYB) using the imaginary time estimator of Ref. [6] (“ τ ”) and the Legendre estimator of Ref. [27] (“Leg”). Middle panel: Zoom with τ data and projection. Right panel: Zoom with Legendre data and projection.

the numerical effort remains negligible compared to the QMC simulation cost for obtaining data. Projections typically take less than a second per iteration on a single core. We provide an implementation of the algorithm in Ref. [31].

Result.

QMC data. We now discuss results of applying the denoising procedure of “Projection algorithm” to the example of quantum Monte Carlo data. We first consider data obtained with the numerically exact hybridization expansion QMC method [6,9]. Methods of this type form the backbone of modern real-materials calculations within DFT + DMFT [32] and are used for understanding minimal models of strongly correlated quantum many-body systems [14]. Numerous generalizations [9,33], improvements, and open source implementations exist [34–37].

We apply the method to the fermionic imaginary time Green’s function of the noninteracting ($U = 0$) half-filled quantum impurity system coupled to a “semicircular” density of states (for details see Appendix B). We calculate

$$G(\tau) = -\text{Tr}[\rho c(\tau)c^\dagger(0)]. \quad (4)$$

This system corresponds to the exact solution of a Bethe lattice model in the infinite coordination number limit [38,39] and is frequently studied in the context of dynamical mean field theory [40]. While the solution for $U = 0$ is available analytically, its simulation within the hybridization expansion requires the statistical sampling of a large number of terms in a diagrammatic expansion.

In the hybridization expansion, $G(\tau)$ can either be estimated using a binning method in imaginary time (we designate this as the “ τ ” estimator [6]) or by expanding the solution into orthogonal polynomials and sampling their coefficients (we designate this the “Legendre” estimator [27]).

Figure 2 shows the improvement that can be obtained by making use of the projection for this model. Results and error bars are obtained from 64 independent Monte Carlo runs. The left panel shows an imaginary-time Green’s function obtained at temperature $T = 1/100$ (we set the hopping parameter to $t = 1$). Data measured with both estimators is consistent with

the exact solution within Monte Carlo error bars (not shown) but Monte Carlo noise is clearly visible. The middle panel shows the same τ estimator data, focused on $8 \leq \tau \leq 12$. The result from the projection of this noisy data is shown as an orange dashed line and is consistent with the exact solution.

The right panel shows the same region for the Legendre estimator. In this case, because the Legendre expansion introduces correlations in imaginary time, the data appears smooth but nevertheless shows considerable deviation from the exact result. Similarly, this deviation is eliminated in the projected data that (within the resolution of the plot) coincides with the exact data.

In Fig. 3, we present a detailed error analysis for the same system, focusing on $G(\beta/2)$ which, at low T , is related to the density of states at the Fermi energy [41]. We show the result from 64 independent evaluations of the two estimators; as

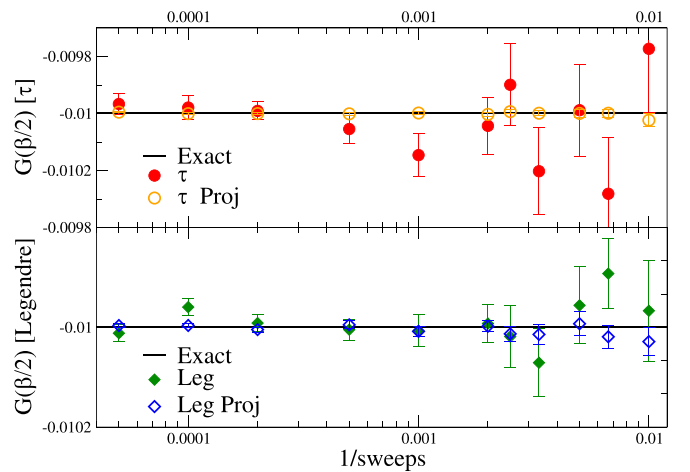


FIG. 3. Monte Carlo error of system of Fig. 2 as a function of sweeps obtained from 64 independent runs. Black and red, top panel: τ estimator of Ref. [6] and projection plotted with error bars. Green and blue, bottom panel: Legendre measurement of Ref. [27]. Note the different y-axis scales.

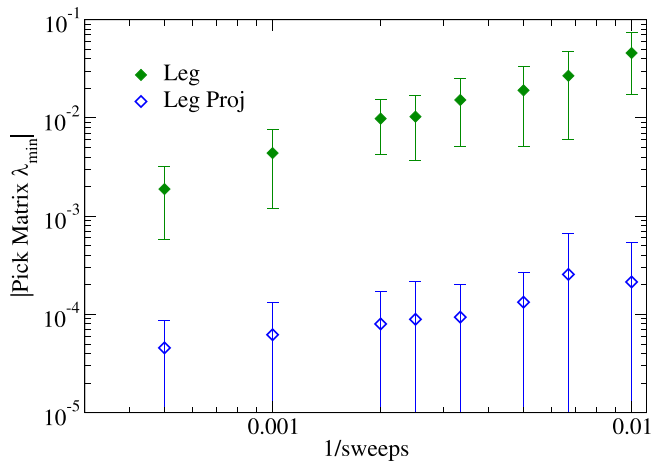


FIG. 4. Average absolute value and error of the lowest eigenvalue of the Pick matrix, calculated from 64 independent Monte Carlo runs, as a function of the inverse number of sweeps. Legendre measurement. Green: Original data. Blue: Data after projection. System as in Fig. 2.

expected from a numerically exact method, when the number of sweeps increases, the estimators approach the exact result.

We next project each of the 64 samples and average the projected Green’s functions. For both estimators, the projected data are consistent with the exact result within error bars for all samples, confirming that the projection did not introduce a bias. For all numbers of sweeps considered, the error bars on the projected $G(\beta/2)$ using the τ estimator are approximately 20 times smaller than those before projection, corresponding to a $20^2 = 400$ -fold saving in CPU time. Similarly, for the Legendre estimator, the average error is reduced by around a factor of five (corresponding to a 25-fold saving in CPU time). For both estimators, this factor remains approximately constant as the number of sweeps is increased.

We note that the projection employed here is highly nonlinear and may in general deform a Gaussian distribution, with details depending on the type of Monte Carlo algorithm and the observable estimator. It is therefore dangerous to perform the projection with just one noisy sample (such as the mean value of a QMC calculation). Rather, a careful statistical analysis using, for example, jackknife or bootstrap error propagation of independent data is advised. In this paper, we first perform the Hankel projection on multiple independent data sets and only then average the results.

Positive spectral functions. Is there a positive spectral function that corresponds to a set of imaginary time points? This question is answered by the Pick criterion [44], which states that if the so-called Pick matrix for Matsubara data is formed, a positive spectral function consistent with the data only exists if the matrix has no negative eigenvalues [22]. See Appendix D for a brief discussion.

The exact solution of a causal quantum problem has a Pick matrix with only non-negative eigenvalues. However, Monte Carlo noise generally introduces negative eigenvalues to the Pick matrix. Figure 4 shows the average of the absolute value of the minimal (i.e. the most negative) eigenvalue λ_{\min} of the Pick matrix constructed from the Legendre data of Fig. 2

(green) and its projection (blue). The projection reduces the magnitude of $|\lambda_{\min}|$ by one to two orders of magnitude on average, demonstrating that the projected data is much closer to a positive spectral function than the original results. The remaining negative contribution may stem from a combination of systematic errors such as the projection convergence cutoff and Fourier transform precision artifacts, as well as from errors that are consistent with the inner product introduced here but inconsistent with causality. Aside from ensuring that the Green’s functions are physical, the existence of a positive spectral function is a prerequisite for obtaining precise analytic continuations with modern methods [22,23,45–47].

Interacting model. The projection method is independent of the algorithm and the system studied and is particularly useful in systems with strong noise, including systems with a sign problem caused by, for example, frustration. The square-lattice Hubbard model with a large next-nearest hopping term $t' = t = 1$ is such a frustrated model. Figure 5 shows the Green’s function of a frustrated four-site cluster at temperature $T = 1/20$, chemical potential $\mu = 0$, and interaction $U = 5$, coupled to a noninteracting bath (see Appendix C). Systems of this type appear in the simulation of “dynamical cluster approximation” (DCA) cluster dynamical mean field problems [42]. The system is solved with a continuous-time [9] auxiliary field [43] quantum impurity solver, using a Green’s function estimator formulated in Matsubara frequency space [5]. The average sign of the problem is ~ 0.63 .

The left panel of Fig. 5 shows the (strictly negative) momentum-space Green’s functions at the three independent momentum points $k = (0, 0)$, $k = (0, \pi)$, and $k = (\pi, \pi)$. The middle panel shows measured data along with the projection for $k = (0, 0)$, and the right panel for $k = (\pi, 0)$. Error bars are shown on every fifth data point.

The improvement of the projection over the measured data is around a factor of two on average (corresponding to a fourfold saving of computer time). The smaller improvement may be due to the different formulation of the Monte Carlo estimator (which measures the Fourier transform of the data shown [5] and therefore already induces strong correlations between time points). Note that the smaller advantage observed here is not due to the sign problem. We have observed cases (not shown) where the Hankel projection offers greater benefits as the temperature is lower and the sign problem becomes more severe.

Discussion. The Hankel projection introduced here is a generic postprocessing method that can be applied to any imaginary-time response function data at negligible additional cost. As we have shown, it removes unphysical components of the noise and thereby leads to data that is much more precise. A careful error analysis has shown that no bias is introduced by the projection, and that projected data is substantially closer to a “causal” solution than unprojected data. Hankel projections of this type should therefore be applicable in all imaginary-time and Matsubara frequency calculations where noise (such as stochastic noise, measurement noise, or approximation errors) is a source of error.

The advantage of the method strongly depends on the type of estimator and Monte Carlo algorithm used. In continuous-time algorithms, where very many independent time points are measured, the method is more effective than in

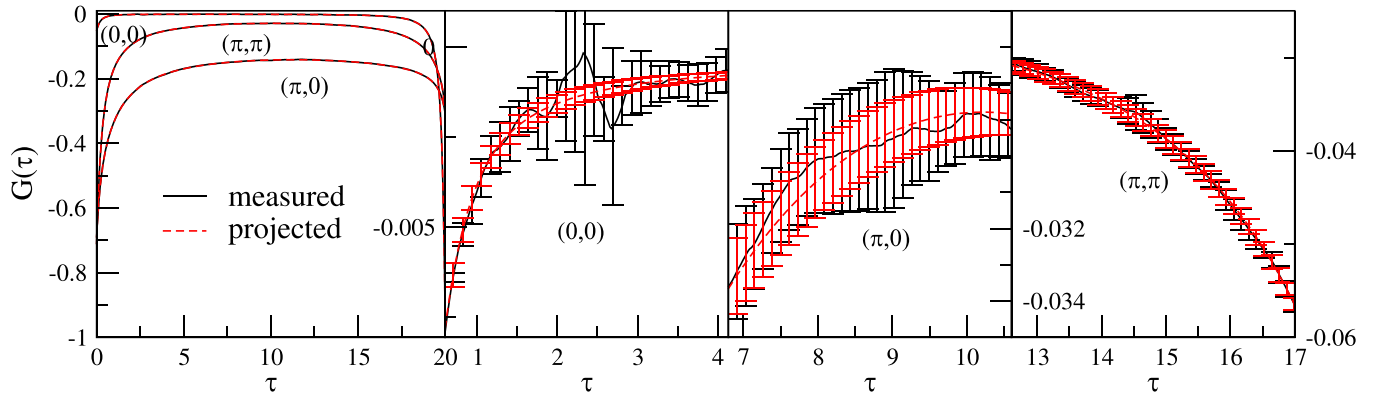


FIG. 5. Projection of a strongly frustrated four-site DCA data cluster [42] as obtained from an auxiliary field continuous-time quantum Monte Carlo (CT-AUX) [43] simulation (black) and Hankel projection (red). Left panel: Green's functions at $(0, 0)$, $(\pi, 0)$, and (π, π) . Middle panel: zoom for $(0,0)$ Green's function. Right panel: zoom for $(\pi, 0)$ Green's function.

discrete-time setups [2,3] where typically only a few correlated imaginary-time slices are measured. Interaction [5,43] and hybridization expansion [6] methods employ different estimators with entirely different error structures and therefore lead to different improvements of the result. Applications to diagrammatic Monte Carlo of various types, such as inchworm Monte Carlo, bold-line Monte Carlo, to matrix-valued correlators, and to bosonic systems [48] will be interesting to explore.

Similarly, it will be interesting to explore if this method can remove unphysical components of Green's functions obtained with methods with systematic approximations, such as certain noncausal vertex-corrected beyond-GW methods [49] or tensor-train approximations [50,51]. In those methods, there is no stochastic “noise” component but a systematic approximation error that may violate causality, which is closely related to the inner product structure discussed in this paper [25].

The data for the figures are submitted as a supplement to this paper [52].

Acknowledgments. We thank A. Erpenbeck and E. Huang for useful comments. Y.Y. was sponsored by NSF QIS 2310182. A.F.K. was supported by the Department of Energy, Office of Basic Energy Sciences, Division of Materials Sciences and Engineering under Grant No. DE-SC0023231. E.G. and C.Y. were supported by the U.S. Department of Energy, Office of Science, Office of Advanced Scientific Computing Research and Office of Basic Energy Science, Scientific Discovery through Advanced Computing (SciDAC) program under Award No. DE-SC0022088.

Appendix A: Dykstra's projection algorithm. Dykstra's algorithm [30] is a method that computes a point in the intersection of convex sets. For a specified initial point, Dykstra's algorithm will find the projection of that initial point onto the intersection. In other words, Dykstra's algorithm will find the point in the intersection that is closest to the initial point.

Suppose we have two convex sets A and B which we know we can do projections onto via operation \mathcal{P}_A and \mathcal{P}_B , and we want to project the initial point x_0 on the intersection

of A and B . We set another two auxiliary variables a, b to store the intermediate updates, where the initial values are $a_0 = b_0 = 0$. Dykstra's algorithm updates the values of these parameters at step $k+1$ according to their value at step k via

$$x_{k+1}^{(a)} = \mathcal{P}_A(x_k - a_k), \quad (\text{A1a})$$

$$a_{k+1} = x_{k+1}^{(a)} - (x_k - a_k), \quad (\text{A1b})$$

$$x_{k+1}^{(b)} = \mathcal{P}_B(x_{k+1}^{(a)} - b_k), \quad (\text{A1c})$$

$$b_{k+1} = x_{k+1}^{(b)} - (x_{k+1}^{(a)} - b_k), \quad (\text{A1d})$$

$$x_{k+1} = x_{k+1}^{(b)}. \quad (\text{A1e})$$

By the end of the calculation, the variables x converge to the intended point of projection. It is obvious that the updates from \mathcal{P}_A [Eqs. (A1a) and (A1b)] are identical to those from \mathcal{P}_B [Eqs. (A1c) and (A1d)], except for their inputs. This allows us to easily adapt the same approach when applying Dykstra's algorithm to more than two convex sets.

In applying Dykstra's algorithm to Hankel projections, we start with an initial Hankel matrix created from a given Green's function. We have four convex sets as detailed in “Method” and “Projection algorithm”. The corresponding projections are as follows:

- (i) Projection onto positive semidefinite (PSD) matrices.
- (ii) Projection onto matrices with specific values at $G(0)$ and $G(\beta)$.
- (iii) Projection onto the entire Hankel matrix, as shown in Fig. 1.
- (iv) Projection onto the small Hankel matrix, outlined with a dashed line in Fig. 1.

These four projections are performed sequentially in a single update of Dykstra's algorithm, similar to projection \mathcal{P}_A and \mathcal{P}_B described above. The process continues until the Hankel matrices from two consecutive iterations are close enough, or until the calculation reaches a maximum number of iterations. At the end of the calculation, the projected Green's function can be directly read from the converged Hankel matrix.

Appendix B: Single impurity coupled to an infinite-dimensional bethe lattice. We study an impurity of two spin degrees of freedom coupled to a bath with a dispersion characterized by a semielliptical form having a bandwidth of $4t$. The corresponding density of states of the bath is given by $D_{\uparrow\downarrow}(\omega) = D_{\downarrow\downarrow}(\omega) = \frac{1}{2\pi t^2} \sqrt{4t^2 - \omega^2}$ for $-2t \leq \omega \leq 2t$, and the hybridization function is expressed as $\Delta_{\uparrow\downarrow}(\tau) = \Delta_{\downarrow\downarrow}(\tau) = -\int d\omega D(\omega) \frac{e^{-\tau\omega}}{1+e^{-\beta\omega}}$ for $0 \leq \tau \leq \beta$. The action of this impurity reads

$$\mathcal{S}_{\text{imp}} = \mathcal{S}_{\text{loc}} + \int_0^\beta d\tau \int_0^\beta d\tau' \sum_{\sigma=\uparrow,\downarrow} c_\sigma^*(\tau) \Delta_{\sigma\sigma}(\tau - \tau') c_\sigma(\tau'), \quad (\text{B1})$$

$$\begin{aligned} \mathcal{S}_{\text{loc}} = & \int_0^\beta d\tau \sum_{\sigma=\uparrow,\downarrow} c_\sigma^*(\tau) (\partial_\tau - \mu) c_\sigma(\tau) \\ & + U \int_0^\beta d\tau c_\uparrow^*(\tau) c_\uparrow(\tau) c_\downarrow^*(\tau) c_\downarrow(\tau). \end{aligned} \quad (\text{B2})$$

The hybridization expansion [6] treats \mathcal{S}_{loc} exactly and performs a perturbation expansion of the hybridization term around this solution.

The dynamical mean field formalism is reviewed in Ref. [40].

Appendix C: DCA model hamiltonian. The DCA data of Fig. 5 are obtained on a four-site cluster approximation to the Hubbard model [42,53,54] on a heavily frustrated square lattice with $t' = t = 1$ as in [55]. Shown are the results for the first iteration at an interaction strength of $U = 5$, starting from the DCA solution of the noninteracting model.

The choice of parameters is motivated by the fact that the frustration $t = t'$ leads to a strong fermion sign problem that drastically amplifies noise. While the projection cannot overcome the exponential cost of the sign problem, it alleviates the size of the noise and therefore the prefactor of the exponential scaling with temperature or interaction.

The DCA formalism is reviewed in Ref. [42].

Appendix D: Pick criterion. In this Appendix, we briefly describe the Pick criterion for Matsubara Green's functions. The criterion is based on work by Pick [44], and was introduced to the context of fermionic Matsubara Green's functions in Ref. [22].

The problem of analytic continuation is to find a function \mathcal{G} ,

$$\mathcal{G} : \mathbb{C} \rightarrow \mathbb{C}, \quad (\text{D1})$$

that is analytic on the upper half of the complex plane, \mathbb{C}^+ , and coincides with the available numerical data G on the Matsubara axis, i.e., $G_n = \mathcal{G}(z = i\omega_n)$. Because \mathcal{G} is to represent a Green's function, it should have an imaginary part with a definite sign. Such a function is called a Nevanlinna function.

A priori it is not known whether a Nevanlinna function exists that passes through numerical data with stochastic or systematic errors. This question, and thus the question of whether a physically correct Green's function (i.e., analytic on \mathbb{C}^+ and with appropriate sign of the spectrum) exists, is answered by the Pick criterion [44]. First, one maps the (closed) upper half complex plane $\overline{\mathbb{C}^+}$ to the (closed) complex unit disk \mathbb{D} via a Möbius transformation:

$$h : \overline{\mathbb{C}^+} \rightarrow \overline{\mathbb{D}}, \quad (\text{D2})$$

$$h(z) := \frac{z - i}{z + i}. \quad (\text{D3})$$

Next, one forms the Pick matrix out of the numerical data G_n and the Möbius-transformed Matsubara frequencies $h(\omega_n)$:

$$\mathcal{P}_{n,m} = \left[\frac{G_n + G_m^*}{1 - h(\omega_n)h(\omega_m)^*} \right], \quad n, m = 1, 2, \dots, M. \quad (\text{D4})$$

Note that the transformation is not strictly necessary, and that a similar matrix can be formulated without the Möbius transformation [45]. The Pick criterion states that a Nevanlinna interpolant exists if and only if \mathcal{P} is positive semidefinite (PSD), and that a unique solution exists if and only if \mathcal{P} is singular. In other words, evaluating the degree to which \mathcal{P} for a given numerical Green's function G fails to be PSD is a measure of the causality violation of a numerical Green's function.

-
- [1] A. Altland and B. D. Simons, *Condensed Matter Field Theory* (Cambridge University Press, Cambridge, 2010).
- [2] R. Blankenbecler, D. J. Scalapino, and R. L. Sugar, Monte Carlo calculations of coupled boson-fermion systems. I, *Phys. Rev. D* **24**, 2278 (1981).
- [3] J. E. Hirsch and R. M. Fye, Monte Carlo method for magnetic impurities in metals, *Phys. Rev. Lett.* **56**, 2521 (1986).
- [4] N. V. Prokof'ev and B. V. Svistunov, Polaron problem by diagrammatic quantum Monte Carlo, *Phys. Rev. Lett.* **81**, 2514 (1998).
- [5] A. N. Rubtsov, V. V. Savkin, and A. I. Lichtenstein, Continuous-time quantum Monte Carlo method for fermions, *Phys. Rev. B* **72**, 035122 (2005).
- [6] P. Werner, A. Comanac, L. de' Medici, M. Troyer, and A. J. Millis, Continuous-time solver for quantum impurity models, *Phys. Rev. Lett.* **97**, 076405 (2006).
- [7] N. Prokof'ev and B. Svistunov, Bold diagrammatic Monte Carlo technique: When the sign problem is welcome, *Phys. Rev. Lett.* **99**, 250201 (2007).
- [8] A. Bazavov, D. Toussaint, C. Bernard, J. Laiho, C. DeTar, L. Levkova, M. B. Oktay, S. Gottlieb, U. M. Heller, J. E. Hetrick, P. B. Mackenzie, R. Sugar, and R. S. Van de Water, Non-perturbative QCD simulations with 2 + 1 Flavors of improved staggered quarks, *Rev. Mod. Phys.* **82**, 1349 (2010).
- [9] E. Gull, A. J. Millis, A. I. Lichtenstein, A. N. Rubtsov, M. Troyer, and P. Werner, Continuous-time Monte Carlo methods for quantum impurity models, *Rev. Mod. Phys.* **83**, 349 (2011).
- [10] G. Cohen, E. Gull, D. R. Reichman, and A. J. Millis, Taming the dynamical sign problem in real-time evolution of quantum many-body problems, *Phys. Rev. Lett.* **115**, 266802 (2015).
- [11] D. Neuhauser, R. Baer, and D. Zgid, Stochastic self-consistent second-order green's function method for correlation energies

- of large electronic systems, *J. Chem. Theory Comput.* **13**, 5396 (2017).
- [12] R. Rossi, Determinant diagrammatic Monte Carlo algorithm in the thermodynamic limit, *Phys. Rev. Lett.* **119**, 045701 (2017).
- [13] B. Winograd, E. Gull, and D. Zgid, Error propagation in the fully self-consistent stochastic second-order green's function method, [arXiv:2009.10048](https://arxiv.org/abs/2009.10048).
- [14] M. Qin, T. Schäfer, S. Andergassen, P. Corboz, and E. Gull, The Hubbard model: A computational perspective, *Annu. Rev. Condens. Matter Phys.* **13**, 275 (2022).
- [15] J. Gubernatis, N. Kawashima, and P. Werner, *Quantum Monte Carlo Methods: Algorithms for Lattice Models* (Cambridge University Press, Cambridge, 2016).
- [16] H. J. Rothe, *Lattice Gauge Theories: An Introduction* (World Scientific Publishing Company, Singapore, 2012).
- [17] G. D. Mahan, *Many Particle Physics* (Springer, New York, 2010).
- [18] L. Mühlbacher and E. Rabani, Real-time path integral approach to nonequilibrium many-body quantum systems, *Phys. Rev. Lett.* **100**, 176403 (2008).
- [19] P. Werner, T. Oka, and A. J. Millis, Diagrammatic Monte Carlo simulation of nonequilibrium systems, *Phys. Rev. B* **79**, 035320 (2009).
- [20] A. Erpenbeck, E. Gull, and G. Cohen, Quantum Monte Carlo method in the steady state, *Phys. Rev. Lett.* **130**, 186301 (2023).
- [21] M. Jarrell and J. Gubernatis, Bayesian inference and the analytic continuation of imaginary-time quantum Monte Carlo data, *Phys. Rep.* **269**, 133 (1996).
- [22] J. Fei, C.-N. Yeh, and E. Gull, Nevanlinna analytical continuation, *Phys. Rev. Lett.* **126**, 056402 (2021).
- [23] L. Zhang and E. Gull, Minimal pole representation and controlled analytic continuation of Matsubara response functions, *Phys. Rev. B* **110**, 035154 (2024).
- [24] C. Charles, E. J. Gustafson, E. Hardt, F. Herren, N. Hogan, H. Lamm, S. Starecheski, R. S. Van de Water, and M. L. Wagman, Simulating \mathbb{Z}_2 lattice gauge theory on a quantum computer, *Phys. Rev. E* **109**, 015307 (2024).
- [25] A. F. Kemper, C. Yang, and E. Gull, Denoising and extension of response functions in the time domain, *Phys. Rev. Lett.* **132**, 160403 (2024).
- [26] M. J. Hyrkäs, D. Karlsson, and R. van Leeuwen, Cutting rules and positivity in finite temperature many-body theory, *J. Phys. A: Math. Theor.* **55**, 335301 (2022).
- [27] L. Boehnke, H. Hafermann, M. Ferrero, F. Lechermann, and O. Parcollet, Orthogonal polynomial representation of imaginary-time green's functions, *Phys. Rev. B* **84**, 075145 (2011).
- [28] N. J. Higham, Computing a nearest symmetric positive semidefinite matrix, *Linear Algebra Appl.* **103**, 103 (1988).
- [29] M. G. Eberle and M. C. Maciel, Finding the closest toeplitz matrix, *Comput. Appl. Math.* **22**, 1 (2003).
- [30] J. P. Boyle and R. L. Dykstra, A method for finding projections onto the intersection of convex sets in Hilbert spaces, in *Advances in Order Restricted Statistical Inference*, edited by R. Dykstra, T. Robertson, and F. T. Wright (Springer, New York, 1986), pp. 28–47.
- [31] See <https://github.com/CQMP/HankelProjection.git> for the C++ implementation of the algorithm, documentation, and examples.
- [32] G. Kotliar, S. Y. Savrasov, K. Haule, V. S. Oudovenko, O. Parcollet, and C. A. Marianetti, Electronic structure calculations with dynamical mean-field theory, *Rev. Mod. Phys.* **78**, 865 (2006).
- [33] P. Werner and A. J. Millis, Hybridization expansion impurity solver: General formulation and application to Kondo lattice and two-orbital models, *Phys. Rev. B* **74**, 155107 (2006).
- [34] B. Bauer, L. D. Carr, H. G. Evertz, A. Feiguin, J. Freire, S. Fuchs, L. Gamper, J. Gukelberger, E. Gull, S. Guertler, A. Hehn, R. Igarashi, S. V. Isakov, D. Koop, P. N. Ma, P. Mates, H. Matsuo, O. Parcollet, G. Pawłowski, J. D. Picon *et al.*, The ALPS project release 2.0: open source software for strongly correlated systems, *J. Stat. Mech.* (2011) P05001.
- [35] P. Seth, I. Krivenko, M. Ferrero, and O. Parcollet, TRIQS/CTHYB: A continuous-time quantum Monte Carlo hybridisation expansion solver for quantum impurity problems, *Comput. Phys. Commun.* **200**, 274 (2016).
- [36] H. Shinaoka, E. Gull, and P. Werner, Continuous-time hybridization expansion quantum impurity solver for multi-orbital systems with complex hybridizations, *Comput. Phys. Commun.* **215**, 128 (2017).
- [37] M. Wallerberger, A. Hausoel, P. Gunacker, A. Kowalski, N. Parragh, F. Goth, K. Held, and G. Sangiovanni, w2dynamics: Local one- and two-particle quantities from dynamical mean field theory, *Comput. Phys. Commun.* **235**, 388 (2019).
- [38] W. Metzner and D. Vollhardt, Correlated lattice fermions in $d = \infty$ dimensions, *Phys. Rev. Lett.* **62**, 324 (1989).
- [39] E. Müller-Hartmann, Correlated fermions on a lattice in high dimensions, *Z. Phys. B* **74**, 507 (1989).
- [40] A. Georges, G. Kotliar, W. Krauth, and M. J. Rozenberg, Dynamical mean-field theory of strongly correlated fermion systems and the limit of infinite dimensions, *Rev. Mod. Phys.* **68**, 13 (1996).
- [41] N. Trivedi and M. Randeria, Deviations from Fermi-liquid behavior above T_c in 2D short coherence length superconductors, *Phys. Rev. Lett.* **75**, 312 (1995).
- [42] T. A. Maier, M. Jarrell, T. Prushke, and M. Hettler, Quantum cluster theories, *Rev. Mod. Phys.* **77**, 1027 (2005).
- [43] E. Gull, P. Werner, O. Parcollet, and M. Troyer, Continuous-time auxiliary-field Monte Carlo for quantum impurity models, *Europhys. Lett.* **82**, 57003 (2008).
- [44] G. Pick, Über die beschränkungen analytischer funktionen durch vorgegebene funktionswerte, *Math. Ann.* **78**, 270 (1917).
- [45] J. Fei, C.-N. Yeh, D. Zgid, and E. Gull, Analytical continuation of matrix-valued functions: Carathéodory formalism, *Phys. Rev. B* **104**, 165111 (2021).
- [46] L. Ying, Analytic continuation from limited noisy Matsubara data, *J. Comput. Phys.* **469**, 111549 (2022).
- [47] Z. Huang, E. Gull, and L. Lin, Robust analytic continuation of Green's functions via projection, pole estimation, and semidefinite relaxation, *Phys. Rev. B* **107**, 075151 (2023).
- [48] L. Pollet, Recent developments in quantum Monte Carlo simulations with applications for cold gases, *Rep. Prog. Phys.* **75**, 094501 (2012).
- [49] G. Stefanucci, Y. Pavlyukh, A.-M. Uimonen, and R. van Leeuwen, Diagrammatic expansion for positive spectral functions beyond GW: Application to vertex corrections in the electron gas, *Phys. Rev. B* **90**, 115134 (2014).

- [50] Y. Núñez Fernández, M. Jeannin, P. T. Dumitrescu, T. Kloss, J. Kaye, O. Parcollet, and X. Waintal, Learning Feynman diagrams with tensor trains, *Phys. Rev. X* **12**, 041018 (2022).
- [51] A. Erpenbeck, W.-T. Lin, T. Blommel, L. Zhang, S. Isakov, L. Bernheimer, Y. Núñez-Fernández, G. Cohen, O. Parcollet, X. Waintal, and E. Gull, Tensor train continuous time solver for quantum impurity models, *Phys. Rev. B* **107**, 245135 (2023).
- [52] See Supplemental Material at <http://link.aps.org/supplemental/10.1103/PhysRevResearch.6.L032042> for the data of the figures.
- [53] M. H. Hettler, A. N. Tahvildar-Zadeh, M. Jarrell, T. Pruschke, and H. R. Krishnamurthy, Nonlocal dynamical correlations of strongly interacting electron systems, *Phys. Rev. B* **58**, R7475 (1998).
- [54] M. Jarrell, T. Maier, C. Huscroft, and S. Moukouri, Quantum Monte Carlo algorithm for nonlocal corrections to the dynamical mean-field approximation, *Phys. Rev. B* **64**, 195130 (2001).
- [55] S. Li and E. Gull, Magnetic and charge susceptibilities in the half-filled triangular lattice Hubbard model, *Phys. Rev. Res.* **2**, 013295 (2020).